

Simulation of Soils Under Rapid Cyclic Loading Conditions

W. Ehlers, M. Schenke and B. Markert

Abstract The stability of structures strongly relies upon the strength and stiffness of the foundation soil underneath. If fluid-saturated or nearly saturated soils are subjected to rapid cyclic loading conditions, for instance, during earthquakes, the intergranular frictional forces might be dramatically reduced. Subsequently, the load-bearing capacity decreases or even vanishes, if the soil grains loose contact to each other. This phenomena is often referred to as soil liquefaction. Drawing our attention to fluid-saturated granular materials with heterogeneous microstructures, the modelling is carried out within a continuum-mechanical framework by exploiting the macroscopic Theory of Porous Media (TPM) together with thermodynamically consistent constitutive equations. In this regard, the present contribution proceeds from a fully saturated soil, composed of an elasto-plastic solid skeleton and a materially incompressible pore fluid. The governing material parameters of the solid skeleton have been identified for the research-unit sand. The underlying equations are used to simulate soils under rapid cyclic loading conditions. In this regard, the semi-infinite domain is split into a near field, which usually the domain of interest, and a far field, which extends the simulated domain towards infinity. In order to avoid wave reflections at the near-field boundaries an energy-absorbing layer is introduced. Finally, several simulations are carried out. Firstly, a parametric study of the particular far-field treatment is performed and, secondly, soil liquefaction is simulated, where the underlying initial-boundary-value problem is inspired by practically relevant scenarios.

W. Ehlers (✉) · M. Schenke
Institute of Applied Mechanics, University of Stuttgart, Stuttgart, Germany
e-mail: ehlers@mechbau.uni-stuttgart.de

B. Markert
Institute of General Mechanics, RWTH Aachen University, Aachen, Germany

1 Introduction

From a continuum-mechanical point of view, granular materials, such as soils, can neither be classified as solids nor fluids. Their macroscopic observed state (solid- or fluid-like) is a direct consequence of the microstructural intergranular frictional forces and, thus, strongly depends on the loading conditions. If fluid-saturated soils are subjected to rapid cyclic loading conditions, depending on the amplitude and the frequency of the excitation, its load-bearing capacity may decrease dramatically causing the soil to exhibit a fluid-like behaviour, i. e. it liquefies. For instance, buildings on the surface may tilt, which is referred to as structural overturning, or even entirely collapse. In the related literature, the general term “liquefaction” comprises more specific liquefaction-related phenomena, in particular, “flow liquefaction” and “cyclic mobility” [1]. The term “flow liquefaction” addresses an instability phenomenon, which is associated with loose soils with a low shear strength. Therein, the intergranular frictional forces are reduced dramatically by an increasing pore pressure until the residual shear strength cannot sustain static equilibrium anymore. In contrast, the term “cyclic mobility” is associated with medium dense to dense soils and refers to a limited plastic deformation under cyclic loading conditions, where the overall stability of the granular assembly is maintained.

When describing liquefaction phenomena, on the one hand, a comprehensive understanding of the mutual interactions of the various components, in particular, the solid skeleton, composed of the grains, and the pore fluid, which itself can be a mixture of various interacting components, is decisive. On the other hand, special attention also needs to be paid to the description of the contractant (densification) and dilatant (loosening) behaviour of the solid skeleton under pure shear deformation, which is a consequence of the sliding and the rolling of the grains. In particular, depending on the initial density, the soil exhibits a macroscopically contractant (loose soil) or dilatant behaviour (medium-dense to dense soil) under shear loading. Note that the dilatant behaviour of medium-dense and dense soils is preceded by a slightly contractant behaviour [2]. As a consequence, medium-dense and dense soils exhibit a contractant behaviour if they are subjected to small shear deformations. In order to explain, soil liquefaction, attention is drawn to a fluid-saturated soil with a low *Darcy* permeability subjected to rapid cyclic shear deformations. Therein, in contrast to a dry soil, the materially incompressible pore fluid (here water) has no time to evacuate from the reducing pore space. As a consequence, an excess of pore pressure accumulates, thereby reducing the intergranular normal forces, and thus, the intergranular frictional forces. Therefore, the load-bearing capacity of the whole fluid-saturated soil is weakened or might be lost entirely.

Aiming at the simulation of liquefaction phenomena, there are several models available (e.g. [3–7]) most of which are based on *Biot*'s theory [8]. However, these models proceed from different approaches in order to describe the behaviour of the solid skeleton. In this regard, some are associated with the Cam-Clay-based descriptions (e.g. [9, 10]) and others with the hypoplasticity framework (e.g. [11]). Furthermore, it is also worth to mention the more phenomenological approaches, such

as [12, 13], which employ a direct stress-strain relation that distinguishes between loading and unloading stages.

The present contribution proceeds from a thermodynamically consistent approach based on the Theory of Porous Media (TPM) (e.g. [14–16]), where the solid skeleton is described as an elasto-plastic material including isotropic hardening and a stress-dependent failure surface. The governing equations comprise the balance equations of [17] and the elasto-plastic solid-skeleton description of [18]. Following this, the governing balance equations are discretised with respect to space and time, thereby accounting for the transient loading conditions. In this regard, the semi-infinite half-space is spatially discretised, by splitting the analysed domain into a near field, which is, in general, the domain of interest, and a far field, which extends towards infinity. However, truncating the semi-infinite half-space at the near field, which is often sufficient in quasi-static simulations, introduces artificial boundaries at which, in a dynamic analysis, the incident waves are reflected back into the domain of interest. In order to overcome this problem, several methods have been proposed in the literature. In general, they can be classified into so-called coupling methods, such as, for instance, the combined finite-element-infinite-element-method (FEM-IEM), and so-called absorbing-boundary-condition (ABC) methods. The present contribution proceeds from the approach proposed in [19]. Therein, the near and the far field are spatially discretised by mixed *Taylor-Hood* finite elements (FE) and infinite elements (IE), respectively, and, additionally, an energy-absorbing layer at the FE-IE interface has been introduced. In the next step, the temporal discretisation is carried out, thereby, accounting for the special requirements of the global (spatial discretisation) and the local system (plastic evolution). In particular, the *Hilber-Hughes-Taylor* method is used for the global system, whereas, the implicit (backward) *Euler* is used for the local system. Following this, the discretised governing equations are implemented into the coupled finite-element solver PANDAS, which is linked to the commercial FE package Abaqus via a general interface. This coupling allows the definition of complex initial-boundary-value problems through Abaqus, thereby using the material models of PANDAS. The material parameters of the solid-skeleton model have been identified for the sand used in the research-unit FOR 1136, by the commonly used *Least-Squares* approximation. The numerical model will be used, firstly, to perform a parametric study of the far-field treatment and, secondly, to simulate flow liquefaction in a loose soil. Finally, future aspects are addressed in the conclusions.

2 Description of the Fluid-Saturated Soil

A suitable framework for the description of fully-saturated soils is provided by the TPM. Following this, the individual components are described separately through their respective mass and momentum balances, but joined together to a holistic formulation by incorporating suitable production terms.

Within the macroscopic TPM approach, one assumes a homogeneous distribution of overlaid individual components φ^α , which, in the present case, are the materially incompressible solid skeleton ($\alpha = S$) and the materially incompressible pore fluid ($\alpha = F$), both within a representative elementary volume (REV) dv . The composition of the bulk volume element is defined through respective volume fractions $n^\alpha = dv^\alpha/dv$, where dv^α is the partial volume of the component φ^α within the REV. Note that the saturation condition $\sum_\alpha n^\alpha = n^S + n^F = 1$ must hold. Following this, two density functions are defined. The material (realistic or effective) density $\rho^{\alpha R} = dm^\alpha/dv^\alpha$ relates the components local mass dm^α to its volume dv^α , while the partial (global or bulk) density $\rho^\alpha = dm^\alpha/dv$ is associated with the bulk volume. Moreover, both density definitions are related to each other through $\rho^\alpha = n^\alpha \rho^{\alpha R}$. As we assume materially incompressible and uncrushable grains, the realistic density of the solid remains constant under the prescribed isothermal conditions, but the bulk density can still change through a changing volume fraction n^α .

In the framework of the TPM, the solid φ^S and the pore fluid φ^F are treated as superimposed continua where each spatial point is simultaneously occupied by particles of both components and each components particle is moving according to its own motion function and, thus, have their own velocity and acceleration field. In this regard, it is convenient to express the solid motion in the *Lagrangean* or material setting through the solid displacement \mathbf{u}_S and the fluid motion in the *Eulerian* or spatial setting through the seepage velocity \mathbf{w}_F relative to the solid motion. Following this, the displacement, velocity and acceleration functions read [17]:

- solid motion: $\mathbf{u}_S = \mathbf{x} - \mathbf{X}_S$, $\mathbf{v}_S = (\mathbf{u}_S)'_S = \dot{\mathbf{x}}_S$, $(\mathbf{v}_S)'_S = \ddot{\mathbf{x}}_S$,
- fluid motion: $\mathbf{w}_F = \dot{\mathbf{x}}_F - \dot{\mathbf{x}}_S$, $(\mathbf{v}_F)'_F \approx (\mathbf{v}_F)'_S$.

$$(1)$$

Therein, \mathbf{X}_S denotes the position of a solid material point in the reference configuration ($t = t_0$), while \mathbf{x} is the position of a point in the current configuration ($t > t_0$). Moreover, $(\cdot)'_S$ and $(\cdot)'_F$ denote material time derivatives following the motion of the solid skeleton and the pore fluid, respectively. Note that according to [8], for the lower frequency range ($f \leq 30$ Hz), which is the case within the scope of the present contribution, the convective terms can be neglected. Thus, $(\mathbf{v}_F)'_F = (\mathbf{v}_F)'_S + \text{grad } \mathbf{v}_F \mathbf{w}_F \approx (\mathbf{v}_F)'_S$.

According to [17], the governing balance equations are the convective-less total momentum balance of the overall porous material, the convective-less momentum balance of the pore fluid and the total volume balance of the overall porous material. They read:

$$\rho^S (\mathbf{v}_S)'_S + \rho^F (\mathbf{v}_F)'_S = \text{div} (\mathbf{T}_E^S - p \mathbf{I}) + (\rho^S + \rho^F) \mathbf{b}, \quad (2)$$

$$\rho^F (\mathbf{v}_F)'_S = \text{div} (-n^F p \mathbf{I}) + \rho^F \mathbf{b} \frac{(n^F)^2 \gamma^{FR}}{k^F} \mathbf{w}_F + p \text{grad } n^F, \quad (3)$$

$$0 = \text{div} (\mathbf{v}_S + \frac{k^F}{\gamma^{FR}} \{ \rho^{FR} [\mathbf{b} - (\mathbf{v}_F)'_S] - \text{grad } p \}). \quad (4)$$

Therein, \mathbf{b} is the unique mass-specific body force, k^F is the hydraulic conductivity (Darcy permeability) and $\gamma^{FR} = g\rho^{FR}$ is the effective fluid weight with $g = |\mathbf{b}| = \text{const.}$ as the scalar gravitational acceleration. Moreover, \mathbf{T}_E^S is the effective solid stress, which is associated with the intergranular forces, p is the pore-fluid pressure and \mathbf{I} is the second-order identity tensor. The corresponding primary variables of the resulting three-field formulation are the solid displacement \mathbf{u}_S , the pore-fluid velocity \mathbf{v}_F and the pore-fluid pressure p .

In order to complete the model, a constitutive description of the effective solid stress \mathbf{T}_E^S is necessary. In extension of [17], which proceeds from a purely elastic description, we continue with an elasto-plastic model, in particular, with an elasto-(visco)plastic solid skeleton including isotropic hardening and a stress-dependent failure surface (cf. [18] for details). Restricting the presentation to the small-strain regime, the linear solid strain tensor is given by

$$\varepsilon_S = \frac{1}{2}(\text{grad } \mathbf{u}_S + \text{grad}^T \mathbf{u}_S) \quad \longrightarrow \quad \varepsilon_S = \varepsilon_{Se} + \varepsilon_{Sp}, \quad (5)$$

which in the framework of elasto-plasticity is additively split into an elastic ε_{Se} and a plastic part ε_{Sp} . Following this, the solid volume fraction can be written as (cf. [20]),

$$n^S = n_{0S}^S(1 - \varepsilon_S^V) = n_{0S}^S(1 - \varepsilon_{Sp}^V)(1 - \varepsilon_{Se}^V) = n_p^S(1 - \varepsilon_{Se}^V). \quad (6)$$

Therein, n_{0S}^S denotes the initial solid volume fraction and $\varepsilon_S^V = \text{div } \mathbf{u}_S = \varepsilon_S \cdot \mathbf{I}$ is the volumetric solid strain, which is split into its corresponding elastic part $\varepsilon_{Se}^V = \varepsilon_{Se} \cdot \mathbf{I}$ and plastic part $\varepsilon_{Sp}^V = \varepsilon_{Sp} \cdot \mathbf{I}$. Note that, as we proceed from a continuum-mechanical framework, in contrast to geomechanics, volumetric compression corresponds to negative volumetric quantities, i.e. $\mathbf{T}_E^S \cdot \mathbf{I} < 0$ and $\varepsilon_S^V < 0$, whereas volumetric expansion corresponds to positive volumetric quantities, i.e. $\mathbf{T}_E^S \cdot \mathbf{I} > 0$ and $\varepsilon_S^V > 0$.

2.1 Elastic Domain

In order to capture the non-linear behaviour of sand, even in the geometrically linear regime, the following stress-strain relation, based on a non-linear elastic potential, has been introduced [18]:

$$\mathbf{T}_E^S = 2\mu^S \varepsilon_{Se}^D + \left[k_0^S + k_1^S \left(\frac{\varepsilon_{Se}^V \text{crit}}{\varepsilon_{Se}^V \text{crit} - \varepsilon_{Se}^V} - 1 \right) \right] \varepsilon_{Se}^V \mathbf{I}. \quad (7)$$

Therein, $\varepsilon_{Se}^D = \varepsilon_{Se} - 1/3 \varepsilon_{Se}^V \mathbf{I}$ denotes the deviator of the elastic strain tensor. Moreover, μ^S is the constant elastic shear modulus, k_0^S and k_1^S are volumetric bulk moduli, and $\varepsilon_{Se}^V \text{crit}$ is the critical volumetric strain, which is given by

$$\varepsilon_{Se \text{ crit}}^V = 1 - \frac{n_{\max}^S}{n_p^S}, \quad (8)$$

where n_{\max}^S is a material parameter defining the densest packing.

2.2 Plastic Domain

Within the framework of elasto-plasticity, the elastic domain is bounded by an appropriate yield surface. For soils, or granular matter in general, a suitable criterion is provided in [21]. It reads:

$$F = \sqrt{\Gamma \mathbb{I}^D + \frac{1}{2} \alpha \mathbb{I}^2 + \delta^2 \mathbb{I}^4 + \beta \mathbb{I} + \epsilon \mathbb{I}^2 - \kappa} = 0, \quad (9)$$

where $\Gamma = (1 + \gamma \frac{\mathbb{III}^D}{(\mathbb{II}^D)^{3/2}})^m$.

Therein, \mathbb{I} , \mathbb{II}^D and \mathbb{III}^D are the first principal invariant of \mathbf{T}_E^S , and the (negative) second and third principal invariants of the effective stress deviator $(\mathbf{T}_E^S)^D$. The material parameter sets $\mathcal{S}_h = (\delta, \epsilon, \beta, \alpha, \kappa)^T$ and $\mathcal{S}_d = (\gamma, m)^T$ define the shape of the yield surface in the hydrostatic (\mathcal{S}_h) and deviatoric plane (\mathcal{S}_d).

Following the concept of non-associated plasticity for frictional geomaterials, a suitable plastic potential, which describes the contractant and dilatant behaviour of the soil, is given by

$$G = \sqrt{\psi_1 \mathbb{II}^D + \frac{1}{2} \alpha \mathbb{I}^2 + \delta^2 \mathbb{I}^4 + \psi_2 \beta \mathbb{I} + \epsilon \mathbb{I}^2}. \quad (10)$$

Therein, ψ_1 and ψ_2 are material parameters, which serve to relate the dilatation angle to experimental data. The flow rule governing the plastic strain rate $(\varepsilon_{Sp})'_S$ reads

$$(\varepsilon_{Sp})'_S = \Lambda \frac{\partial G}{\partial \mathbf{T}_E^S}. \quad (11)$$

Therein, Λ is the so-called plastic multiplier, which in the framework of viscoplasticity using the overstress concept of *Perzyna* [22] is determined from

$$\Lambda = \frac{1}{\eta} \left\langle \frac{F}{\sigma_0} \right\rangle^r, \quad (12)$$

where $\langle \cdot \rangle$ are the *Macaulay* brackets, η is the relaxation time, σ_0 is the reference stress and r is the viscoplastic exponent. Note that the overstress concept also regularises ill-posed problems, for instance during the onset of shear bands (cf. [23] and the references therein), through a careful choice of the parameters η and r .

Any dilatant or compactive behaviour of soils is accompanied by macroscopic softening or hardening effects resulting in a shrinkage or an expansion of the yield surface in the principal stress space. Therefore, suitable evolution laws $(p_i)'_S$ for the parameter subset $p_i \in \{\beta, \delta, \epsilon, \gamma\}$ of the yield surface are used (cf. [20]):

$$(p_i)'_S = (p_i^V)'_S + (p_i^D)'_S = (p_i^* - p_i)[C_{pi}^V (\epsilon_{Sp}^V)'_S + C_{pi}^D \|(\epsilon_{Sp}^D)'_S\|],$$

where $p_i(t = 0) = p_{i0}$. (13)

Note that the yield-surface-parameter evolution is split into volumetric $(p_i^V)'_S$ and deviatoric parts $(p_i^D)'_S$, which are driven by the corresponding volumetric and deviatoric plastic strain rates, $(\epsilon_{Sp}^V)'_S$ and $(\epsilon_{Sp}^D)'_S$. Moreover, p_{i0} and p_i^* denote the yield-surface parameters at the initial and the saturated state, respectively, where the latter are associated with the failure surface.

Having cyclic loading conditions in mind, one has to take care of the mutual interlocking of the grains as a consequence of a preloading and their release during a subsequent reloading at a lower isotropic stress state. This influence has been observed during triaxial experiments and is considered in the model through a stress-dependent failure surface (cf. [18] for details)

$$\epsilon^*(\mathbf{I}) = \epsilon_0^*(1 + C_\epsilon \mathbf{I}) \quad \text{with} \quad \epsilon^* \geq \epsilon_{lim}^*. \quad (14)$$

Therein, C_ϵ is a constant evolution parameter of the failure surface, ϵ_0^* theoretically defines the failure surface for the unloaded virgin material and ϵ_{lim}^* defines the limit of the failure-surface parameter.

3 Numerical Treatment

3.1 Spatial Discretisation

The spatial discretisation of the semi-infinite domain is based on the finite-element method (FEM). In this connection, following a variational approach of *Bubnov-Galerkin*-type, the governing strong forms are multiplied by test function and are integrated over the spatial domain yielding the weak forms. However, in contrast to the standard FEM, the semi-infinite halfspace is spatially split into the near field (domain of interest) and far field (extension towards infinity) discretised by finite elements (FE) and infinite elements (IE), respectively.

At first, the attention is drawn to the spatial discretisation of the near field, which is carried out by the FEM. Therein, the governing strong forms (2)–(4) are multiplied with the test functions $\delta \mathbf{u}_S$, $\delta \mathbf{v}_F$ and δp and are integrated over the spatial domain Ω . The particular weak forms are taken from [17] and read

$$\begin{aligned}
0 &= \int_{\Omega} \delta \mathbf{u}_S \cdot \{ \rho^S (\mathbf{v}_S)'_S + \rho^F (\mathbf{v}_F)'_S - (\rho^S + \rho^F) \mathbf{b} \} dv \\
&\quad + \int_{\Omega} \mathbf{grad} \delta \mathbf{u}_S \cdot (\mathbf{T}_E^S - p \mathbf{I}) dv - \int_{\Gamma_I} \delta \mathbf{u}_S \cdot \bar{\mathbf{t}} da,
\end{aligned} \tag{15}$$

$$\begin{aligned}
0 &= \int_{\Omega} \delta \mathbf{v}_F \cdot [\rho^F (\mathbf{v}_F)'_S - \mathbf{b}] dv + \int_{\Omega} \delta \mathbf{v}_F \cdot [\frac{(n^F)^2 \gamma^{FR}}{k^F} \mathbf{w}_F - p \mathbf{grad} n^F] dv \\
&\quad + \int_{\Omega} \mathbf{div} \delta \mathbf{v}_F (-n^F p) dv + \int_{\Gamma_{t^F}} \delta \mathbf{v}_F \cdot \bar{\mathbf{t}}^F da,
\end{aligned} \tag{16}$$

$$\begin{aligned}
0 &= - \int_{\Omega} \mathbf{grad} \delta p \cdot \frac{k^F}{\gamma^{FR}} \{ \rho^{FR} [\mathbf{b} - (\mathbf{v}_F)'_S] - \mathbf{grad} p \} dv + \int_{\Omega} \delta p \mathbf{div} \mathbf{v}_S dv \\
&\quad + \int_{\Gamma_v} \delta p \bar{v} da.
\end{aligned} \tag{17}$$

Therein, $\bar{\mathbf{t}} = (\mathbf{T}_E^S - p \mathbf{I}) \mathbf{n}$ and $\bar{\mathbf{t}}^F = -n^F p \mathbf{n}$ denote the external loading vectors acting on the *Neumann* boundaries Γ_I and Γ_{t^F} of the overall aggregate and the pore fluid, respectively, and $\bar{v} = n^F \mathbf{w}_F \cdot \mathbf{n}$ is the volume efflux draining through the *Neumann* boundary Γ_v with \mathbf{n} as the outward oriented unit surface normal.

In contrast to the near field, the far field is discretised via infinite elements (IE). Additionally, in order to achieve energy-absorbing properties, dashpots are introduced at the FE-IE interface. This procedure is often referred to as visco-damped boundaries (VDB) and originates from [24]. According to [19], the governing weak form, composed of a quasi-static and a viscous damped part, is given by

$$\underbrace{\int_{\Omega} \mathbf{grad} \delta \mathbf{u}_S \cdot (\mathbf{T}_E^S - p \mathbf{I}) dv - \int_{\Omega} \delta \mathbf{u}_S \cdot \rho \mathbf{b} dv}_{\text{quasi-static part}} + \underbrace{\int_{\Gamma_I} \delta \mathbf{u}_S \cdot \mathbf{r} da}_{\text{visous-damped part}} = 0 \tag{18}$$

$$\text{where } \mathbf{r} = \mathbf{P}^T \begin{bmatrix} a \rho c_p & 0 \\ 0 & b \rho c_s \\ 0 & b \rho c_s \end{bmatrix} \mathbf{P} (\mathbf{u}_S)'_S.$$

Therein, $\rho = \sum_{\alpha} \rho^{\alpha}$ denotes the density of overall aggregate, Ω denotes the volume of the infinite element, Γ_I the area of the FE-IE interface and \mathbf{P} a projection matrix relating the global solid velocity components to the local coordinate system (normal and shear direction) on Γ_I . Furthermore, \mathbf{r} represents an area-weighted 3-dimensional force vector containing the nodal contributions of the dashpots to the nodes associated with the area at the FE-IE interface. They depend on the compression- and shear-wave velocities, $c_p = \sqrt{(2\mu_S + \lambda_S)/\rho}$ and $c_s = \sqrt{\mu_S/\rho}$ (cf. [19]), and on the dimensionless compression- and shear-wave damping coefficients a and b .

In a second step, the unknown fields ($\mathbf{u}_S, \mathbf{v}_F, p$) and the corresponding test functions ($\delta\mathbf{u}_S, \delta\mathbf{v}_F, \delta p$) of the weak forms (15–18) are approximated by suitable test and ansatz functions, which, in the present scope, for the sake of stable solution procedure, need to fulfil the *inf-sup* condition (*Ladyshenskaya-Babuška-Brezzi* (LBB) condition) [25]. In particular, \mathbf{u}_S and $\delta\mathbf{u}_S$ are approximated by quadratic shape functions, whereas linear shape functions are used for $\mathbf{v}_F, p, \delta\mathbf{v}_F$ and δp . Note that the test and ansatz functions of the finite and the infinite elements are not given here, instead, the interested reader is referred to [26, 27] for the FE and IE approximation, respectively.

Following this, the spatially discretised formulation combining the near and the far field can be summarised as

$$\mathbf{F}^h = \begin{bmatrix} \mathbf{G}^h(t, \mathbf{y}, \mathbf{y}', \mathbf{y}'', \mathbf{q}) \\ \mathbf{L}^h(t, \mathbf{q}, \mathbf{q}', \mathbf{y}) \end{bmatrix} = \begin{bmatrix} \mathbf{M}\mathbf{y}'' + \mathbf{C}\mathbf{y}' + \mathbf{k}(\mathbf{y}, \mathbf{q}) - \mathbf{f} \\ \mathbf{A}\mathbf{q}' + \mathbf{r}(\mathbf{q}, \mathbf{y}) \end{bmatrix} \stackrel{!}{=} \mathbf{0}. \quad (19)$$

Therein, $\mathbf{y} = [\hat{\mathbf{u}}_S, \hat{\mathbf{v}}_F, \hat{\mathbf{p}}]^T$ is a vector containing the nodal degrees of freedom of the finite-element mesh (global system \mathbf{G}^h) and a vector $\mathbf{q} = [\varepsilon_{Sp}, \Lambda, \mathbf{p}]^T$, which gathers the internal variables plastic strains (ε_{Sp}), plastic multiplier (Λ) and yield-surface evolution parameters (\mathbf{p}) at the *Gauss* points of the finite-element mesh (local system \mathbf{L}^h). Note that for the sake of convenience the abbreviation $(\cdot)' = (\cdot)'_S$ is used. Moreover, \mathbf{M} and \mathbf{C} are the generalised mass and damping matrices, $\mathbf{k}(\mathbf{y}, \mathbf{q})$ and $\mathbf{r}(\mathbf{y}, \mathbf{q})$ denote the static residual vectors of the global and local system, respectively, and \mathbf{f} is the generalised force vector acting on the *Neumann* boundaries.

3.2 Temporal Discretisation

In the next step, the temporal discretisation of Eq. (19) is carried out. In order to account for the specific requirements regarding numerical properties (e.g. stability, numerical damping) of the global and the local system, different time-integration schemes are deployed. In particular, the global system benefits from a numerical-damping-free procedure, whereas unconditional stability is desired for the local system.

In this regard, \mathbf{G}^h is discretised through the implicit *Hilber-Hughes-Taylor* (HHT) method (cf. [28]) which is a generalisation of *Newmarks* method (cf. [29]) but allows for the explicit control of the numerical damping. Note that the for dynamic problems desired explicit schemes, which are more efficient, are not applicable within the current setting, as the incompressibility of the constituents leads to a singular and, thus, a non-invertible mass matrix (cf. [17] for details). The time-discrete form of Eq. (19)₁ is given by

$$\begin{aligned}
& \mathbf{M} \mathbf{y}_{n+1}'' + (1 + \alpha)(\mathbf{C} \mathbf{y}_{n+1}' + \mathbf{k}(\mathbf{y}_{n+1}, \mathbf{q}_{n+1}) - \mathbf{f}_{n+1}) \\
& \quad - \alpha(\mathbf{C} \mathbf{y}_n' + \mathbf{k}(\mathbf{y}_n, \mathbf{q}_n) - \mathbf{f}_n) \stackrel{!}{=} \mathbf{0} \\
\text{with } & \mathbf{y}_{n+1} = \mathbf{y}_n + \Delta t \mathbf{y}_n' + \Delta t^2 \left(\left(\frac{1}{2} - \beta \right) \mathbf{y}_n'' + \beta \mathbf{y}_{n+1}'' \right), \\
& \mathbf{y}_{n+1}' = \mathbf{y}_n' + \Delta t \left((1 - \gamma) \mathbf{y}_n'' + \gamma \mathbf{y}_{n+1}'' \right).
\end{aligned} \tag{20}$$

Therein, the parameter α controls the numerical damping, on the one hand, by adding the quasi-static residual contributions from the previous state (at t_n) to the current residual (at t_{n+1}) and, on the other hand, by the parameters β and γ , which are inherit from *Newmarks* method, and are given by

$$\beta = \frac{1}{4}(1 - \alpha)^2, \quad \gamma = \frac{1}{2}(1 - \alpha). \tag{21}$$

A suitable choice of the parameter α ranges from $\alpha = -1/3$ (significant damping) to $\alpha = 0$ (no damping), whereby, in the latter, the trapezoidal rule ($\beta = 1/4$, $\gamma = 1/2$) is obtained. Note that a value of $\alpha = -0.05$ is in general considered as good choice as the inevitably time-stepping-induced high-frequency noise is quickly removed without a significant effect on the low-frequency response of the system.

The local system \mathbf{L}^h , in order to ensure unconditional stability, the implicit (backward) *Euler* scheme is exploited. In this regard, the time-discrete representation of (19)₂ is given by

$$\mathbf{A} \mathbf{q}_{n+1}' + \mathbf{r}(\mathbf{q}_{n+1}, \mathbf{y}_{n+1}) \stackrel{!}{=} \mathbf{0} \quad \text{with} \quad \mathbf{q}_{n+1}' = \frac{\mathbf{q}_{n+1} - \mathbf{q}_n}{\Delta t}. \tag{22}$$

3.3 Solution Procedure

The solution of the coupled system (19) is carried out with respect to its block-structured nature through a generalisation of the Block *Gauß-Seidel-Newton* method, which is also know as multilevel or, in this particular case, as two-stage *Newton* method. This procedure results in two nested *Newton* iterations. In this connection, at each global iteration, which seeks the solution of the global variables \mathbf{y}^{n+1} , the nonlinear local system is iteratively solved for the internal variables \mathbf{q}_{n+1} at each *Gauss* integration point with frozen global variables (e.g. cf. [30] and reference therein).

The discretised system is implemented into the FE package PANDAS¹ and linked through a general interface to the commercial FE package Abaqus [31]. This coupling

¹Porous media Adaptive Non-linear finite-element solver based on Differential Algebraic Systems, www.get-pandas.com.

allows for the definition of complex initial-boundary-value problems in terms of features, such as kinematic coupling and tie constraints, and in terms of large-scale analyses through parallelisation.

4 Parameter Identification

In order to identify the solid-skeleton material parameters for the sand of the research-unit FOR 1136 the course of actions is basically following the procedure described in [18]. Therein, a staggered identification scheme has been carried, in which, at first, the elastic shear modulus μ_S and the compression-extension-ratio parameter of the failure surface γ^* are determined straightforward from triaxial loading-unloading loops and from compression and extension experiments at different confining pressures. The remaining model parameters are found through a minimisation of the squared error between simulation and experiment, which is commonly known as *Least-Squares* optimisation method. In particular, a gradient-based constrained optimisation is used, in which the *Hessian* matrix is approximated through BGFS (Broyden, Fletcher, Goldfarb, Shannon) (cf. [32] and references) and the parameter constraints are considered via the sequential-quadratic-programming (SQP) technique [33]. The identified solid-skeleton material parameters of the research-unit sand FOR 1136 are summarised in the Appendix.

5 Simulations

5.1 Parametric Studies

The following section addresses several parametric studies related to the numerical treatment of the semi-infinite unbound-domain. In particular, in the first investigation the macroscopic damping properties of a fully-saturated soil, which is mainly governed by the *Darcy* permeability, is investigated. The second set of studies serves as a parametric study of the present far-field treatment, in particular, of its energy-absorbing capabilities in relation to certain wave types. In this regard, as the following simulation are solely related to the elastic wave-propagation problem, the elasto-plastic solid is simplified to a purely elastic material governed by the material parameters given in Table 1. Note that the material parameters μ_S and k_s^0 are chosen arbitrarily and result in comparatively low compression- and shear-wave propagation velocities. The remaining material parameters, in particular, k^F and γ^{FR} , are defined in the related sections.

Table 1 Material parameters of the numerical parametric study of the far-field treatment

μ^S	k_S^0	k_S^1	ρ^{SR}	ρ^{FR}	n_{0S}^S
0.26 m ² /MN	0.40 m ² /MN	0.0 m ² /MN	2700 kg/m ³	1000 kg/m ³	0.6

5.1.1 Parametric Study of the Damping Characteristics of a Fluid-Saturated Soil

When subjecting a soil to rapidly changing loading conditions waves are emitted at the source and propagate through the domain. The resulting, in general, complex particle motion can be considered as a superposition of two fundamental wave types, in particular, compression or primary waves (p-waves) and shear or secondary waves (s-waves). By the assumption of a purely elastic solid and by neglecting viscous shear forces within the pore fluid, its macroscopic observed damping properties are solely related to the solid-skeleton-pore-fluid interaction, in particular, to the solid-fluid momentum exchange (cf. Eq. 3). Therein, the momentum exchange is mainly driven by the solid volume fraction, $n^S = 1 - n^F$, and, thus, by the volumetric deformations (cf. Eq. 6). As deviatoric deformations do not provide significant volumetric strains within the small strain regime, the dissipative properties due to pure shear deformations can be neglected in the following parametric study. Hence, the damping-property study is solely applied to compression waves.

In this regard, the displacement amplitude of the solid skeleton is investigated at different depths with varying *Darcy*-permeability. Note that the specific pore-fluid weight is set to $\gamma^{FR} = 10^4$ N/m³. The underlying initial-boundary-value problem (IBVP) is depicted in Fig. 1 (left). Therein, a 3-dimensional soil column, which as simplified to a 1-d problem via suitable boundary conditions, is subjected to a displacement impulse applied on the top of the soil column given by

$$\bar{u}(t) = \bar{u}_0 \sin(2\pi t/T_0)[H(t) - H(t - \tau)] \quad (23)$$

with $T_0 = 1$ s, $\tau = T_0/2$, $\bar{u}_0 = 5 \cdot 10^{-3}$ m and $H(t - \tau)$ as the *Heaviside* step function.

The evolution of the solid-skeleton displacement amplitude of the triggered p-wave for different *Darcy* permeabilities $k^F = \{10^{-1}, 10^{-3}, 10^{-3}\}$ m/s is depicted in Fig. 1 (right). It can be seen that with decreasing permeability, which increase the viscous friction between the soil grains and the pore fluid, the amplitude of the compression wave reduces rapidly. Thus, already for a relatively high *Darcy* permeability of $k^F = 10^{-3}$ m/s, the influence of the p-wave can be neglected already one meter below the surface.

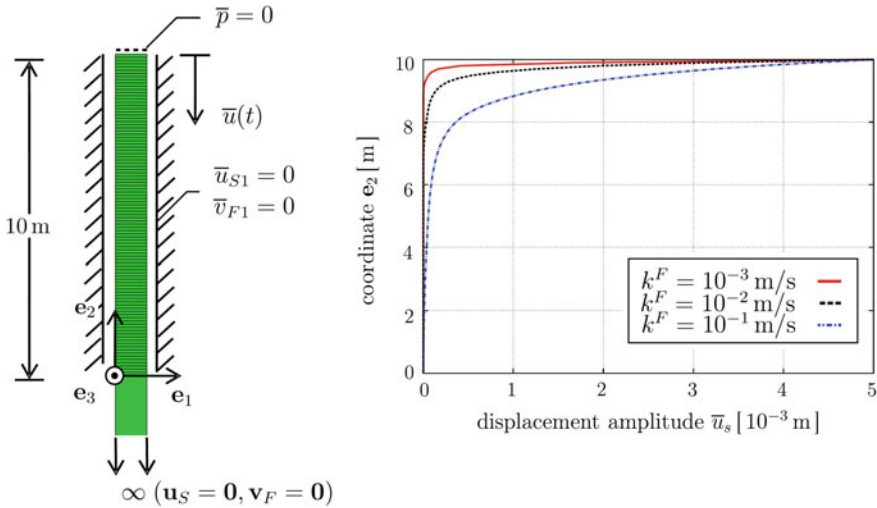
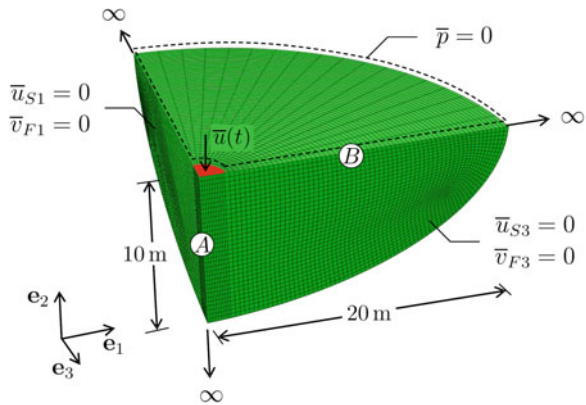


Fig. 1 IBVP to investigate the influence of the Darcy permeability on the p-wave penetration depth

Fig. 2 Initial-boundary-value problem of the far-field-treatment parametric study

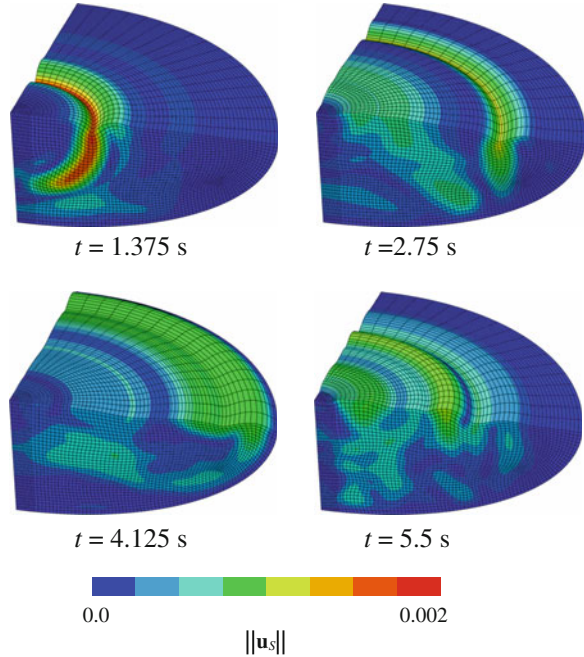


5.1.2 Parametric Study of Numerical Far-Field Treatment

The second example addresses a parametric study of the far-field treatment. In particular, the influence of the damping coefficients and of the quasi-static contribution on the energy-absorbing capabilities are investigated. The governing IBVP is depicted in Fig. 2.

Therein, a ellipsoidal domain (first and second minor axis: 20 m, third minor axis: 10 m) is extended towards infinity by use of infinite elements, whereas the FE-IE interface is described through viscous-damped boundaries. Note that the infinite elements are not depicted in Fig. 2. The resulting numerical model consists of approximately 40,000 elements, which results in approximately 700,000 degrees of

Fig. 3 Contour plot of the magnitude of the solid displacement $\|\mathbf{u}_s\|$ on the deformed geometry (scale factor: 500) of the truncated semi-infinite halfspace

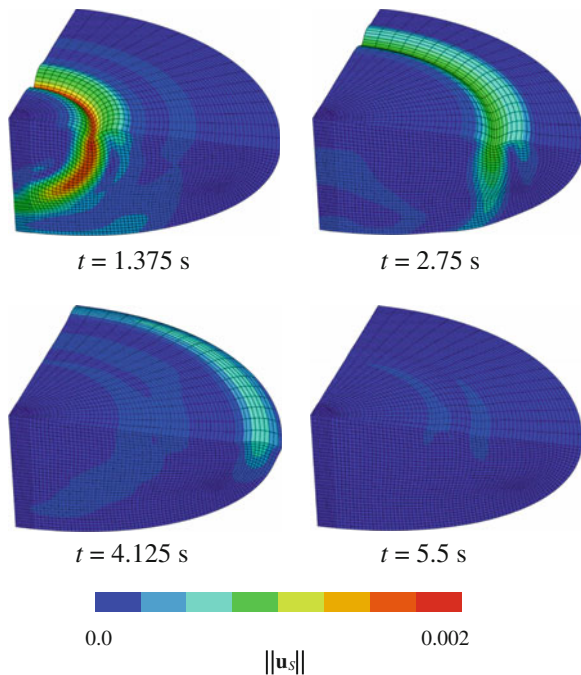


freedom. Thus, due to the problem size, the simulations have been carried out in parallel on 40 cores. In order to trigger waves propagating through the domain, a displacement impulse, given by Eq. (23), is applied at the indicated area. Moreover, in order to judge the energy-absorbing capabilities, the vertical displacements of the solid skeleton at A (located at a depth of 5 m) and B (located 10 m from the vertical symmetry line) are evaluated.

In order to keep this parametric study within more general setting, the damping properties of the VDB with respect to compressional waves are investigated as well, although they are, as seen before, not relevant for most practical-oriented geotechnical scenarios. Thus, to allow for the induced wave to propagate nearly without a loss through the domain, the *Darcy* permeability and the specific weight are set to $k^F = 10^{-2}$ m/s and $\gamma^{FR} = 10^{-4}$ N/m³, respectively. Note that, hereby, the quasi-static contribution has been neglected and the normal and shear damping coefficients are set to $a = b = 1$.

The impact on the numerical solution of the specific far-field treatment is qualitatively illustrated in Figs. 3 and 4. The displacement impulse on top of the domain triggers a compression and a surface wave (*Rayleigh* wave) which, in case of the truncated domain, is reflected at introduced artificial domain boundaries (cf. Fig. 3). In contrast, using the special far-field treatment composed of infinite elements and an energy-absorbing layer at the near-field-far-field transition shows a significant improvement (cf. Fig. 4).

Fig. 4 Contour plot of the magnitude of the solid displacement $\|\mathbf{u}_s\|$ on the deformed geometry (scale factor: 500) of the semi-infinite halfspace incorporating VDB



5.1.3 Influence of the Damping Coefficients

The following simulations investigate the influence of the normal- and shear-damping coefficients, a and b , of the dashpots at the FE-IE interface on the energy-absorption behaviour. In particular, the proposed values of Lysmer and Kuhlemeyer (LK) [24] ($a = b = 1$), which give the best energy absorption if the wave-propagation direction is normal to the FE-IE interface, is compared to the approach of White et al. [34], which is based on the maximisation of the dissipated energy over different wave incidence angles. In the latter approach, the damping coefficients are computed via

$$a = \frac{8}{15\pi}(5 + 2c - 2c^2), \quad b = \frac{8}{15\pi}(3 + 2c) \quad \text{where} \quad c = \sqrt{\mu^S / (\lambda^S + 2\mu^S)}. \quad (24)$$

By use of the material parameters of Table 1, the damping coefficients can be computed as $a = 0.93$ and $b = 0.69$. Note that the quasi-static contribution (cf. Eq. 18) has been neglected.

The results of the simulation are depicted in Fig. 5. Therein, the gray line is used as a reference (ref.) showing the result of the truncated domain. It can be seen that the approach of White et al. (W) gives slightly better results compared to Lysmer and Kuhlemeyer (LK). However, as the approach of White et al. is exploiting the linear elastic *Hooke* an law for the constitutive description of the solid, their proposal is tied

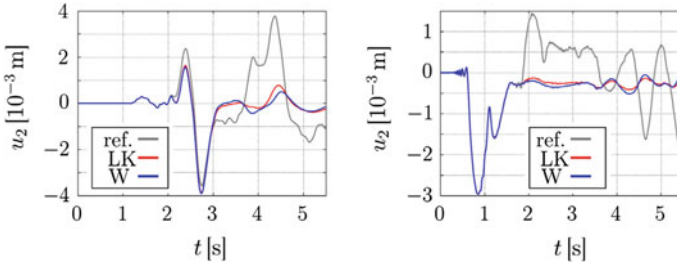


Fig. 5 Evolution of the vertical displacement of A (*right*) and B (*left*) for different damping parameters

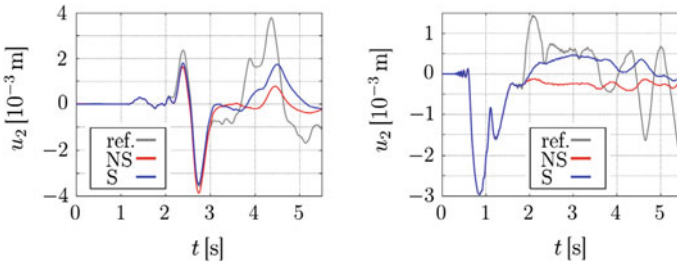


Fig. 6 Evolution of the vertical displacement of A (*right*) and B (*left*) for the quasi-static-contribution-influence study

to the first and second *Lamé* constants and, thus, may not be suitable for arbitrary solid material descriptions.

5.1.4 Influence of the Quasi-Static Contribution

The second example studies the influence of the quasi-static contribution. In this regard, a simulation involving the quasi-static contribution (S) is compared to a simulation without one (NS). Note that the damping parameters are set to $a = b = 1$.

The results of the simulation are depicted in Fig. 6. It can be seen that the best energy-absorbing capabilities are obtained if the quasi-static part is neglected (NS), which is in accordance with [35]. However, if the simulation contains quasi-static loading steps, for instance, if the transient load is preceded by a consolidation step, the quasi-static contribution has to be considered, as it provides the necessary residual stiffness to the far-field.

5.2 Liquefaction of Loose Sand

The next example is related to the simulation of flow liquefaction in a loose, water-saturated sand under cyclic loading conditions, which is a common scenario, for instance, during earthquakes.

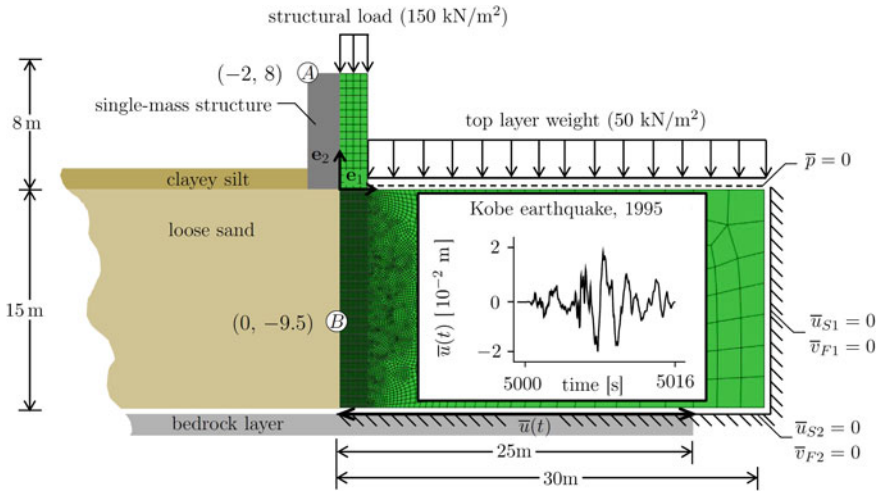


Fig. 7 Geometry (*left*) and deduced initial-boundary-value problem (*right*) of the liquefaction examples

The initial-boundary-value problem under consideration is inspired by the liquefaction-prone Wildlife Refuge area in Imperial Valley in southern California, where the layout of the domain of interest is as follows (Fig. 7, left). From top to bottom, the soil layers are a clayey silt, a liquefiable sand, a stiff clay and a bedrock layer. Based on that, a suitable numerical model is deduced (Fig. 7, right), where the weight of the single-mass structure and the top layer are replaced by uniformly distributed loads of 150 and 50 kN/m², respectively. Note that the replacement of the top layer by its corresponding load, avoids numerical difficulties as it ensures that the domain below is under compression during the simulation. Below that is a layer of a liquefiable sand, which is described as an elasto-(visco)plastic material with isotropic hardening and a stress-dependent failure-surface (cf. Sect. 2). The bedrock layer at the bottom of the modelled domain is subjected to lateral displacements according to the records of the Kobe earthquake in 1995 in Japan, which have been logged at the FUK station. Note that the modelled semi-infinite halfspace has been truncated without the use of a special far-field treatment. Due to the facts that, on one hand, the prescribed bedrock-layer displacements mainly initiate shear waves and that, on the other hand, the fluid-saturated soil exhibits significant damping properties with respect to compression waves, the size of the numerical problem size has been reduced, by discarding a special far-field treatment. Note that the finite-element mesh below structure has been refined in order to account for the expected strain localisation. Moreover, tie constraints have been imposed at the interface between the structure and the foundation soil to ensure kinematic compatibility. The resulting numerical model consists of approximately 24,000 elements with approximately 110,000 degrees of freedom.

Table 2 Comparison of the solid-skeleton material parameters for medium-dense FOR 1136 sand (set 1) to the estimated parameters for a loose sand (set 2)

Material	n_{0S}^S	ψ_1	ψ_2
Medium-dense FOR 1136 sand (1)	0.61	1.3	0.53
Loose sand (2)	0.4	0.4	0.1

The loading history of the liquefaction problem can be split into two stages. At first, the structural and top layer weights are applied in an initialisation step ($0 \text{ s} < t < 5000 \text{ s}$). Note that during that stage, the permeability is increased from $k^F = 10^{-5} \text{ m/s}$ to $k^F = 10^{-3} \text{ m/s}$ in order to speed up the consolidation process and to ensure a static equilibrium before proceeding with the second step ($5000 \text{ s} < t < 5016 \text{ s}$), in which the displacement of the bedrock layer is prescribed according to the records of the Kobe earthquake.

Note that in order to trigger liquefaction phenomena with the available material parameters, the prescribed displacements are scaled up by a factor of 15. Moreover, the material parameters of the medium-dense FOR 1136 sand are modified in order to describe a loose sand. In particular, the initial solid volume fraction n_{0S}^S and the material parameters governing the dilatation angle, ψ_1 and ψ_2 , are varied such that liquefiable-prone loose sand can be mimicked (cf. Table 2). The initial solid volume fraction n_{0S}^S and the material parameters governing the dilatation angle, ψ_1 and ψ_2 , are varied such that liquefiable-prone loose sand is mimicked (cf. Table 2).

A time sequence of contour plots of the norm of the accumulated plastic strain tensor $\|\varepsilon_{Sp}\|$ on the deformed finite-element mesh (unscaled) are depicted in Fig. 8. It clearly illustrates the failure of the loose soil foundation beneath the structure. This particular failure mode is known as punching shear failure [36].

As mentioned earlier, soil liquefaction is consequence of the pore-pressure build-up due to the contractant tendency of the soil, which reduces the intergranular normal forces, and thus, the intergranular frictional forces. To make this point clearer, the interplay between the pore pressure p and the effective volumetric solid stress $\mathbf{T}_E^S \cdot \mathbf{I}$, which is associated with the intergranular normal forces, is plotted at point B in Fig. 9 (left).

As can be seen due to the rapid cyclic motions that the slight pore-pressure build-up, approximately till $t \approx 5006 \text{ s}$, continues to a dramatic pore-pressure increase resulting in a drop of the negative volumetric solid stress, which corresponds, according to the continuum-mechanical framework, to a decrease of the intergranular normal forces, and thus, reduces the intergranular frictional forces. Note that the effective volumetric solid stress may take slight positive values, which is non-physical in a cohesionless soil, but owed to the elasticity law (7) in case of positive volumetric solid strains. As a consequence of the reduced intergranular frictional forces, the foundation soil liquefies and does not recover into a static equilibrium any more. This is also illustrated in Fig. 9 (right), where the vertical displacement of point A located on top of the single-mass structure is depicted. Therein, the collapse of the

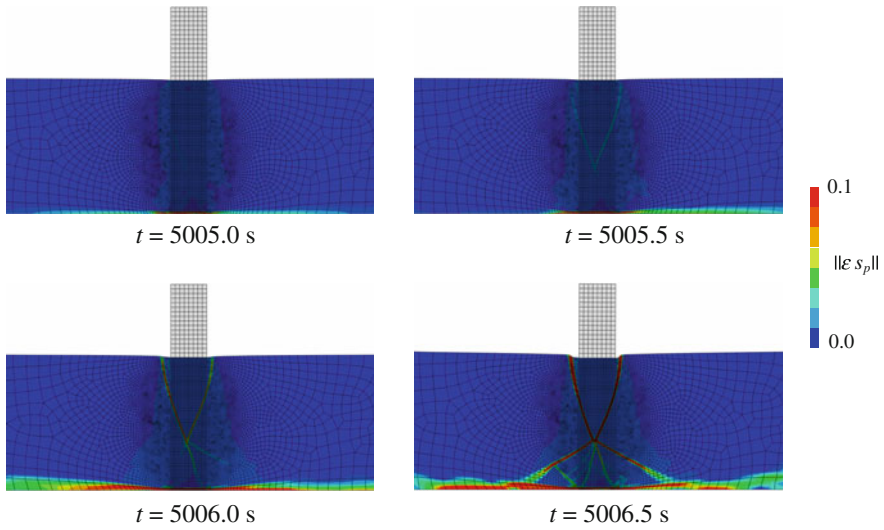


Fig. 8 Contour plots of the norm of the accumulated plastic strain tensor $\|\varepsilon_{Sp}\|$ on the deformed mesh (scale factor: 5) at different times illustrating flow liquefaction

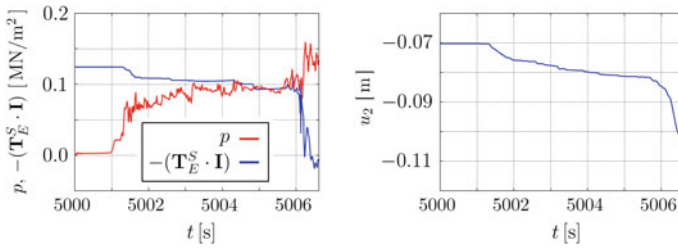


Fig. 9 Evolution of the pore pressure p and the effective volumetric solid stress $\mathbf{T}_E^S \cdot \mathbf{I}$ at point B (left) and the time history of the vertical displacement of point A (right) in the case of flow liquefaction

soil foundation is easily recognised by the rapidly increasing vertical displacement of the single-mass structure.

The computation terminates at approximately $t \approx 5006.5$ s due to extremely distorted finite elements located in the developing shear bands beneath the structure.

6 Conclusions

In this contribution, a modelling approach for the prediction of liquefaction phenomena in saturated soils has been presented. The underlying fluid-saturated soil model proceeds from a geometrically linear description based on the macroscopic TPM

Table 3 Elastic material parameters and initial solidity

μ^S	k_0^S	k_1^S	n_{max}^S	n_{0S}^S
190 MN/m ²	20 MN/m ²	47 MN/m ²	0.61	0.623

Table 4 Initial and saturation values of the parameters of the yield surface

δ_0	ϵ_0	β_0	γ_0	δ^*	ϵ_0^*	β^*	γ^*
0.0009 m ² /MN	0.1 m ² /MN	0.05	0	0.001 m ² /MN	0.01 m ² /MN	0.255	1.75

Table 5 Parameters of the yield-surface evolution and the failure surface

C_δ^V	C_ϵ^V	C_β^V	C_γ^V	C_δ^D	C_ϵ^D	C_β^D	C_γ^D	C_ϵ^*	ϵ_{lim}^*
-93 m ² / MN	-150 m ² / MN	-250	0	23 m ² / MN	200 m ² / MN	180	20	0.4 m ² / MN	0.0001

Table 6 Additional yield surface, plastic potential and viscoplastic evolution parameters

κ	α	m	ψ_1	ψ_2	η	r	σ_0
0.0001 m ² /MN	0.01 m ² /MN	0.54	1.3	0.53	0.001 s	1.5	0.0001 MN/m ²

framework involving an elasto-(visco)plastic solid skeleton with isotropic hardening and a stress-dependent failure surface. The presented numerical results reveal the capability of the model to mimic the relevant physical behaviour necessary for the modelling of liquefaction phenomena under rapid cyclic loading conditions. In particular, the model accounts for the behaviour of granular assemblies undergoing volumetric strains under pure shear deformation and resulting in pore-pressure build-up, which reduces the intergranular frictional forces, and thus, the strength of the whole soil. However, as the model has so far only been tested under rapid cyclic loading conditions, statements regarding the behaviour under quasi-static cyclic loading conditions can not be made yet. This will be part of ongoing investigations.

Appendix: Material Parameters of the Elasto-Plastic Solid Describing Medium-Dense FOR 1136 Sand

Below the solid-skeleton material parameters of the research-unit sand FOR 1136² are summarised (Tables 3, 4, 5 and 6).

²Grain size: 0.1–1 mm; sieve retention: $d_{10} = 0.4$ mm, $d_{60} = 0.6$ mm.

References

1. Castro, G., Poulos, S.J.: Factors affecting liquefaction and cyclic mobility. *ASCE. J. Geotech. Eng. Div.* **103**, 501–506 (1977)
2. Casagrande, J.: The determination of the preconsolidation load and its practical significance. In: *Proceedings 1st International Conference on Soil Mechanics and Foundation Engineering* (1936)
3. Lin, C.-H., Borja, R.I.: Technical Report No. 137. The John A. Blume Earthquake Engineering Center, Stanford (2000)
4. Prevost, J.H.: Nonlinear transient phenomena in soil media. *Mech. Eng. Mater.* **30**, 3–18 (1982)
5. Prevost, J., Elgamal, A.M., Abdel-Ghaffar, A.M.: Earthquake-induced plastic deformation of earth dams. In: *Proceedings: 2nd International Conference on Soil Dynamics and Earthquake Engineering*, vol. 4, pp. 9–17 (1985)
6. Zienkiewicz, O.C., Bettles, P.: *Soil Mechanics—Transient and Cyclic Loads*. Wiley, Chichester (1982)
7. Zienkiewicz, O.C., Shiomi, T.: Dynamic behaviour of saturated porous media: the generalized Biot formulation its numerical solution. *Int. J. Numer. Anal. Meth. Eng.* **8**, 71–96 (1984)
8. Biot, M.A.: Theorie of propagation of elastic waves in a fluid-saturated porous solid. *J. Acoust. Soc. Am.* **28**, 168–178 (1956)
9. Manzari, M.T., Dafalias, Y.F.: A critical state two-surface plasticity model for sands. *Geotechnique* **47**, 255–272 (1997)
10. Roscoe, K.H., Burland, J.B.: On the generalized stress-strain behaviour of wet clay. In: Heyman, J., Leckie, F.A. (eds.) *Engineering Plasticity*. Cambridge University Press, Cambridge (1968)
11. Wichtmann, T., Niemunis, A., Triantafyllidis, T.: Strain accumulation in sand due to cyclic loading: drained cyclic tests with triaxial extension. *Soil Dyn. Earthq. Eng.* **27**, 42–48 (2006)
12. Zienkiewicz, O.C., Chan, A.H.C., Pastor, M., Schrefler, B.A.: *Computational Mechanics—with Special Reference to Earthquake Engineering*. Wiley, Chichester (1998)
13. Zienkiewicz, O.C., Chang, C.T., Hinton, E.: Non-linear seismic response and liquefaction. *Int. J. Numer. Anal. Meth. Eng.* **2**, 381–404 (1978)
14. Bowen, R.M.: Incompressible porous media models by use of the theory of mixtures. *Int. J. Eng. Sci.* **18**, 1129–1148 (1980)
15. De Boer, R.: *Theory of Porous Media*. Springer, Berlin (2000)
16. Ehlers, W.: Foundation of multiphasic and porous materials. In: Ehlers, W., Bluhm, J. (eds.) *Porous Media: Theory, Experiments and Numerical Applications*, pp. 3–86. Springer, Berlin (2002)
17. Markert, B., Heider, Y., Ehlers, W.: Comparison of monolithic and splitting solutions schemes for dynamic porous media problems. *Int. J. Numer. Meth. Eng.* **82**, 1341–1383 (2010)
18. Ehlers, W., Avci, O.: Stress-dependent hardening and failure surface of dry sand. *Int. J. Numer. Anal. Meth. Geomech.* **37**, 787–809 (2012)
19. Heider, Y., Markert, B., Ehlers, W.: Dynamic wave propagation in infinite saturated porous media half spaces. *Comput. Mech.* **49**, 319–336 (2012)
20. Ehlers, W., Scholz, B.: An inverse algorithm for the identification and the sensitivity analysis of the parameters governing elasto-plastic micropolar granular material. *Arch. Appl. Mech.* **77**, 911–931 (2007)
21. Ehlers, W.: A single-surface yield function for geomaterials. *Arch. Appl. Mech.* **65**, 246–259 (1995)
22. Perzyna, P.: Fundamental problems in viscoplasticity. *Adv. Appl. Mech.* **9**, 243–377 (1966)
23. Ehlers, W., Graf, T., Ammann, M.: Engineering issues of unsaturated soil. In: Brinkgreve, R.B.J., Schad, H., Schweiger, H.F., Willand, E. (eds.) *Geotechnical Innovations (Studies in Honour of Prof. Dr.-Ing. Pieter Vermeer on Occasion of his 60th Birthday)*. Verlag Glückauf, Essen, pp. 505–540 (2004)
24. Lysmer, J., Kuhlemeyer, R.L.: Finite dynamic model for infinite media. *ASCE. J. Eng. Div.* **95**, 859–877 (1969)

25. Brezzi, F., Fortin, M.: *Mixed and Hybrid Finite Element Methods*. Springer, New York (1991)
26. Marques, J.M.M.C., Owen, D.R.J.: Infinite elements in quasi-static materially nonlinear problems. *Comput. Struct.* **18**, 739–751 (1984)
27. Zienkiewicz, O.C., Taylor, R.L., Zhu, J.Z.: *The Finite Element Method—Its Basis and Fundamentals*. McGraw-Hill, New York (2005)
28. Hilber, H.M., Hughes, T.J.R., Taylor, R.L.: Improved numerical dissipation for time integration algorithms in structural dynamics. *Earthq. Eng. Struct. Dyn.* **3**, 283–292 (1977)
29. Newmark, N.M.: A method of computation of structural dynamics. *ASCE. J. Eng. Div.* **85**, 67–94 (1959)
30. Karajan, N.: An extended biphasic description of the inhomogeneous and anisotropic intervertebral disc, dissertation: Rep. No.: 09-II-19. Dissertation thesis, Report No. II-19, Institute of Applied Mechanics (Civil Engineering), University of Stuttgart (2009)
31. Schenke, M., Ehlers, W.: On the analysis of soils using an abaqus-PANDAS interface. *Proc. Appl. Math. Mech.* **11**, 431–432 (2011)
32. Spellucci, P.: *Numerische Verfahren der nichtlinearen Optimierung*. Birkhäuser, Basel (1993)
33. Spellucci, P.: A new technique for inconsistent QP problems in the SQP-method. *Math. Meth. Oper. Res.* **47**, 335–400 (1998)
34. White, W., Vallianppan, S., Lee, I.K.: Unified boundary for finite dynamic models. *ASCE. J. Eng. Div.* **103**, 949–964 (1977)
35. Häggblad, B., Nordgren, G.: Modelling nonlinear soil-structure interaction using interface elements, elastic-plastic soil elements and absorbing infinite elements. *Comput. Struct.* **26**, 307–324 (1987)
36. Day, R.W.: *Geotechnical Earthquake Engineering Handbook*. Mcgraw-Hill, New York (2002)